

A boundary integral equation method for wave scattering in periodic structures via the Floquet-Bloch transform[☆]

Wangtao Lu^{a,*}, Kuanrong Shen^a and Ruming Zhang^b

^aSchool of Mathematical Sciences, Zhejiang University, Hangzhou, Zhejiang, China

^bInstitute of Mathematics, TU Berlin, 10623 Berlin, Berlin, Germany

ARTICLE INFO

Keywords:

Wave scattering problems
Periodic structures
Floquet-Bloch transform
Boundary integral equations

ABSTRACT

This paper is concerned with the problem of an acoustic wave scattering in a locally perturbed periodic structure. As the total wavefield is non-quasi-periodic, effective truncation techniques are pursued for high-accuracy numerical solvers. We adopt the Green's function for the background periodic structure to construct a boundary integral equation (BIE) on an artificial curve enclosing the perturbation. It serves as a transparent boundary condition (TBC) to truncate the unbounded domain. We develop efficient algorithms to compute such background Green's functions based on the Floquet-Bloch transform and its inverse. Spectrally accurate quadrature rules are developed to discretize the BIE-based TBC. Effective algorithms based on leap and pullback procedures are further developed to compute the total wavefield everywhere in the structure. A number of numerical experiments are carried out to illustrate the efficiency and accuracy of the new solver. They exhibit that our method for the non-quasi-periodic problem has a time complexity that is even comparable to that of a single quasi-periodic problem.

1. Introduction

Due to their powerful and flexible abilities in manipulating waves, periodic structures have seen wide-ranging applications across acoustics, electromagnetics (optics), elastodynamics, and so on. These practical needs highly pursue fast and accurate numerical simulations for the underlying mathematical models. Nevertheless, challenges from geometries of the structures and radiation behaviors of the scattered waves make rigorous mathematical theories and effective numerical solvers equally difficult to establish in practice [4]. Scattering problems in periodic structures have thus been a hot research topic in communities such as engineering, scientific computing and applied mathematics, in the past decades. This paper studies an acoustic wave scattering in a two-dimensional periodic structure with or without local perturbations. Throughout the rest of this paper, we always assume that the periodic structures are sandwiched by two homogeneous media in the transverse direction that is perpendicular to the periodic directions.

The fundamental problem of a plane wave scattered by a periodic structure has been studied intensively among the existing literature. The total wavefield is quasi-periodic so that the problem can be reduced onto a single unit cell. Moreover, the quasi-periodicity leads to Rayleigh expansions of the total wavefield, yielding transparent boundary conditions (TBCs) terminating the transverse direction. Such a boundary value problem has been proved to be well-posed at all wave frequencies except a countable number of frequencies [3]. Readers are referred to [7] for a rigorous proof of the existence of ill-posed frequencies, the so-called embedded eigenmodes or bound states in the continuum (BIC), and also to [13] and the references therein for the extensive applications of BICs.

Suppose the periodic structure is piecewise homogeneous and the quasi-periodic problem is well-posed for a given frequency. Among the existing solvers, the boundary integral equation (BIE) methods are attractive and competitive for such a scattering problem, mainly because they formulate the problem on the boundaries of homogeneous domains, thereby reducing the problem dimensionality by one. Existing BIE methods can generally be classified into two approaches. The first approach represents the wavefield using single or double-layer potentials that rely on quasi-periodic Green's functions [5]. Radiation conditions at infinity are automatically satisfied and BIEs are established on bounded surfaces only. The main difficulty is the evaluation of the complicated quasi-periodic Green's functions, especially when the frequency lies in the vicinity of Rayleigh anomalies in the sense that plane waves propagating horizontally appear in the Rayleigh expansions, and the quasi-periodic Green's functions are not well defined! Readers

^{*}Corresponding author

 wangtaolu@zju.edu.cn (W. Lu); kuanrongshen@zju.edu.cn (K. Shen); ruming.zhang@tu-berlin.de (R. Zhang)
ORCID(s):

are referred to [8, 27] for effective algorithms for evaluating the quasi-periodic Green's functions and for more details of the difficulty. The second approach uses free-space Green's functions, simpler and ready to use, to establish BIEs. As these Green's functions are not quasi-periodic, BIEs are established on the boundaries of homogeneities in a unit cell, which always contain irregular corners/edges [21, 24]. Therefore, the main difficulty comes from the discretizations of the BIEs. Fortunately, high-accuracy techniques for discretizing BIEs on piecewise smooth curves have been well-established [1, 10] so that the second approach becomes arguably more promising at least for 2D problems. Readers are referred to [4] for various numerical solvers for such quasi-periodic problems.

When the periodic structure contains local perturbations or the incident wave is not quasi-periodic, the total wavefield is not quasi-periodic anymore. It becomes a fundamental barrier against an effective numerical solver to accurately truncate the unbounded domain. With perfectly matched layers (PMLs) [6] truncating the transverse direction [9] in advance, existing truncation techniques for periodic structures in closed waveguides including TBCs established by Riccati equations [16, 25], recursively doubling procedures [26, 11, 23], or Bloch-mode expansions [12, 15], become applicable. We point out, in [25], we firstly developed a PML-based BIE solver for wave scattered by a locally perturbed periodic curve, which can attain a high-order accuracy; meanwhile, we have found in [30, 31] that the PML convergence rate may degrade from exponential to algebraic at or close to half-integer wavenumbers (for 2π -period structures), thereby reducing its overall efficiency. Probably, the most effective approach should be attributed to the method of Floquet-Bloch (FB) transform. The wavefield is transformed as an integral of quasi-periodic waves [18], each of which can be computed effectively via the aforementioned solvers. Nevertheless, if the periodic structure contains a local perturbation, a nonlinear map making the structure periodic again has to be sought first [19] to make the FB transform method applicable. The map complicates the governing equations and significantly undermines the efficiency of the FB transform, not to mention that such a map may not even exist if the perturbation destroys the original topology. Motivated from the above, this paper uses the FB transform to construct a TBC without introducing any nonlinear map, and develops an effective BIE solver to compute the non-quasi-periodic total wavefield.

To clarify the underlying methodology, we focus only on a periodic array of sound-soft obstacles with a local perturbation; periodic structures with different physical properties or different topologies may induce guided modes and will be studied separately in a future work. First, we develop a high-accuracy BIE method, following [21], to compute the quasi-periodic Green's function of the background periodic structure for any quasi-periodic parameter. Integrating these quasi-periodic Green's functions based on a special quadrature for the inverse FB (IFB) transform, we develop a fast algorithm to compute the background Green's function and its derivatives excited by any source point in the periodic structure. By sampling source points on a sufficiently regular curve surrounding the local perturbation, the exciting background Green's functions can be exploited to construct a BIE, in terms of single- and double-layer integral operators on the regular curve. The BIE serves as a TBC to truncate the unbounded domain. We further derive BIEs on boundaries of all homogeneities in the truncated domain. The classical kernel-splitting technique in [10] with spectrally accurate quadratures therein is readily adapted here to treat the singularities of the background Green's functions, discretize all BIEs, and establish the final linear system for the unknown wavefield in the truncated region. By horizontally propagating the quasi-periodic Green's functions, the background Green's functions in other unit cells, away from the perturbation, can be easily evaluated by the IFB transform. This allows us to design two effective procedures, leap and pullback, to compute the wavefield everywhere in the whole structure. We carry out a number of numerical experiments to demonstrate that the proposed method can achieve uniform accuracy no matter the input frequency is half-integer or not, thus outperforming the PML truncation method [25]. Moreover, as the quasi-periodic Green's functions are evaluated at the boundaries of homogeneities in a single unit cell for sources on the artificial curve only, the new solver for the non-quasi-periodic problem exhibits a fully comparable time complexity to that of one single quasi-periodic problem.

The rest of this paper is organized as follows. In section 2, we present a mathematical formulation of the scattering problem. In section 3, based on the Floquet-Bloch theory, we present a BIE formulation to compute quasi-periodic Green's functions, and design effective algorithms to compute the background Green's function. In section 4, we use the background Green's function to construct a TBC, that truncates the original problem, and design effective algorithms to compute the total wavefield. Numerical experiments are carried out in section 5, followed by some concluding remarks in section 6 finally.

2. Problem formulation

As illustrated in Figure 1(a), in the two dimensional space \mathbb{R}^2 with the standard Cartesian coordinates $(x_1, x_2)^T$, let a

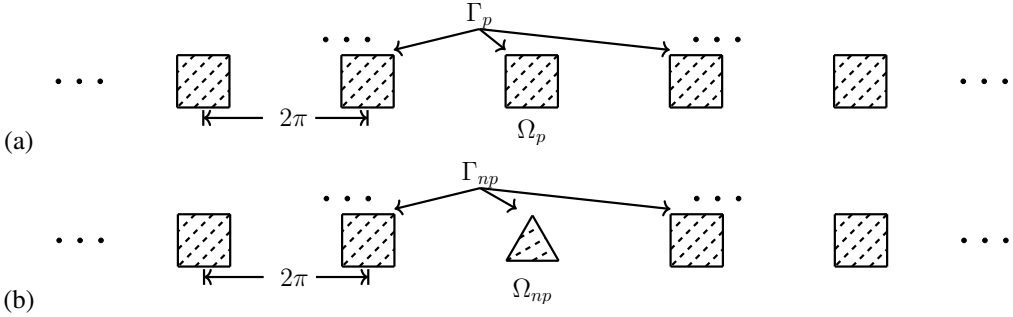


Figure 1: (a): A 2π -periodic structure with a periodic domain Ω_p ; (b): A non-periodic structure with domain Ω_{np} that locally perturbs Ω_p .

periodic array of sound-soft obstacles, with period 2π along the x_1 -direction, be embedded in a homogeneous medium that occupies the unbounded periodic domain Ω_p . The boundary of Ω_p , denoted by Γ_p , consists of the boundaries of all obstacles. Suppose the periodic structure is locally perturbed, as shown in Figure 1(b), where one obstacle is deformed; perturbations with locally different physical properties can be studied similarly. We denote the exterior non-periodic domain by Ω_{np} , which is a local perturbation of Ω_p , and let Γ_{np} be its boundary. To simplify the presentation, we assume that the perturbed region lies in $|x_1| < \pi$, and all obstacles are separated by the vertical lines $x_1 = m\pi$, $m \in \mathbb{Z}$.

Suppose an acoustic wave of wavenumber $k > 0$ is incident in Ω_{np} upon the sound-soft obstacles. The total wavefield u^{tot} is governed by the 2D Helmholtz equation:

$$\Delta u^{\text{tot}} + k^2 u^{\text{tot}} = 0, \quad \text{in } \Omega_{np}, \quad (1)$$

subject to the homogeneous Dirichlet condition:

$$u^{\text{tot}} = 0, \quad \text{on } \Gamma_{np}, \quad (2)$$

where $\Delta = \partial_{x_1}^2 + \partial_{x_2}^2 \in \Omega_{np}$ is the 2D Laplace operator. Let $x = (x_1, x_2)^T$ be a generic point in Ω_{np} . We will consider two different types of incident waves: (i) a plane incident wave $u^{\text{inc}}(x) = e^{ik(\cos \theta x_1 - \sin \theta x_2)}$ with the incident angle $\theta \in (0, \pi)$; (ii) a cylindrical incident wave $u^{\text{inc}}(x; x^*) = \Phi(x, x^*) := \frac{i}{4} H_0^{(1)}(k|x - x^*|)$ excited by a source at a point $x^* = (x_1^*, x_2^*) \in \Omega_{np}$.

For the plane-wave incidence (i), let $u_{\text{ref}}^{\text{tot}}(x)$ denote the quasi-periodic total wavefield for the unperturbed structure Ω_p . If no propagation modes exist for the periodic structure under consideration, Hu and Kirsch [14] proved that the perturbed wavefield $u^{\text{og}} := u^{\text{tot}} - u_{\text{ref}}^{\text{tot}}$ satisfies the following Sommerfeld radiation condition (SRC)

$$\lim_{j \rightarrow \infty} \left\| \frac{\partial u^{\text{og}}}{\partial \nu} - ik u^{\text{og}} \right\|_{H^{-1/2}(B_{a_j})} = 0, \quad (3)$$

where the strictly increasing sequence $\{a_j\}$ is chosen such that $B_{a_j} := \{x : x_1^2 + x_2^2 = a_j^2\} \subset \Omega_{np}$ and $a_j \rightarrow \infty$ as $j \rightarrow \infty$. Note that $u_{\text{ref}}^{\text{tot}}$ is easy to compute numerically because of its quasi-periodicity [21]. For the cylindrical incidence (ii), equation (1) should be modified to

$$\Delta u^{\text{tot}} + k^2 u^{\text{tot}} = -\delta(x - x^*), \quad \text{in } \Omega_{np}, \quad (4)$$

In fact, $u^{\text{tot}}(x; x^*)$ represents the Green's function excited by the source point x^* for the perturbed structure. Unlike the plane-wave incidence, u^{tot} satisfies the SRC condition (3) under the assumption that no propagation modes exist [14].

The SRC condition (3) enables us to derive a BIE-based TBC for u^{og} to truncate the unbounded domain (c.f. Eq. (46)), using the background Green's function for the unperturbed structure.

3. Background Green's function

For a generic source point $x^s \in \Omega_p$, the background Green's function $G(x; x^s)$ is defined as the solution of

$$\Delta G(x; x^s) + k^2 G(x; x^s) = -\delta(x - x^s), \quad \text{in } \Omega_p, \quad (5a)$$

$$G(x; x^s) = 0, \quad \text{on } \Gamma_p, \quad (5b)$$

under the SRC condition (3). As shown in Figure 2, let $C_j = ((2j-1)\pi, (2j+1)\pi) \times \mathbb{R}$ and $\Omega_p^j := C_j \cap \Omega_p$ be the j -th unit cell for $j \in \mathbb{Z}$. Moreover, we denote the boundary of the j -th obstacle by $\Gamma_p^j = C_j \cap \Gamma_p$. Without loss of generality,

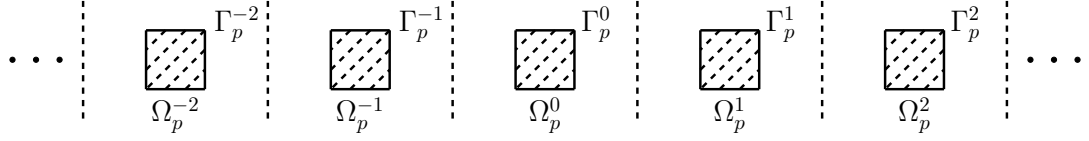


Figure 2: The unbounded homogeneous domain Ω_p^j and the sound-soft obstacle boundary Γ_p^j in the j -th unit cell for $j \in \mathbb{Z}$.

we assume $x^s \in \Omega_p^0$, which corresponds to the perturbed region.

To evaluate the non-quasi-periodic $G(x; x^s)$, we apply the FB transform to express $G(x; x^s)$ as an integral of quasi-periodic Green's functions.

3.1. Floquet-Bloch transform and quasi-periodic Green's function

We recall some basic concepts of the FB transform first. For any compactly supported function $\varphi \in C_0^\infty(\Omega_p)$ with $\varphi|_{\Gamma_p} = 0$, a one-dimensional FB transform \mathcal{J} in the x_1 -direction is defined as

$$(\mathcal{J}\varphi)(\alpha, x) := \sum_{j \in \mathbb{Z}} \varphi\left(x + \begin{pmatrix} 2\pi j \\ 0 \end{pmatrix}\right) e^{2i\pi j \alpha}, \quad x \in \Omega_p; \alpha \in \mathbb{R}, \quad (6)$$

where α is called the FB parameter. Clearly, $\psi := \mathcal{J}\varphi$ belongs to $C^\infty([-1/2, 1/2] \times \Omega_0)$ and is supported in the x_2 -direction. For a fixed $\alpha \in [-1/2, 1/2]$, ψ is α -quasiperiodic in x_1 with period 2π in the sense that

$$\psi\left(\alpha, \begin{pmatrix} x_1 + 2\pi \\ x_2 \end{pmatrix}\right) = e^{2i\pi\alpha} \psi\left(\alpha, \begin{pmatrix} x_1 \\ x_2 \end{pmatrix}\right), \quad \forall x \in \Omega_p, \quad (7)$$

and for a fixed $x \in \Omega_p$, ψ is 1-periodic in α , i.e., $\psi(\alpha + 1, x) = \psi(\alpha, x)$ for any $\alpha \in [-1/2, 1/2]$. Furthermore, integrating ψ w.r.t. the FB parameter α over $(-1/2, 1/2)$ reproduces φ , inducing the IFB transform \mathcal{J}^{-1} defined as

$$(\mathcal{J}^{-1}\psi)(x) := \varphi(x) = \int_{-1/2}^{1/2} \psi(\alpha, x) d\alpha, \quad x \in \Omega_p.$$

For properties of \mathcal{J} and \mathcal{J}^{-1} in weaker functional spaces, we refer readers to [18] for further details.

Now, let $G^{qp}(\alpha, x; x^s) := (\mathcal{J}G)(\alpha, x; x^s)$, and we shall also denote it by $G_\alpha^{qp}(x; x^s)$ when emphasizing its dependence on x . Applying the FB transform to both sides of (5), G^{qp} is governed by

$$\Delta G_\alpha^{qp}(x; x^s) + k^2 G_\alpha^{qp}(x; x^s) = -\delta(x - x^s), \quad \text{in } \Omega_p^0, \quad (8a)$$

$$G_\alpha^{qp}(x; x^s) = 0, \quad \text{on } \Gamma_p^0, \quad (8b)$$

$$G_\alpha^{qp}((\pi, x_2)^T; x^s) = e^{2i\pi\alpha} G_\alpha^{qp}((-\pi, x_2)^T; x^s), \quad x_2 \in \mathbb{R}, \quad (8c)$$

$$\partial_{x_1} G_\alpha^{qp}((\pi, x_2)^T; x^s) = e^{2i\pi\alpha} \partial_{x_1} G_\alpha^{qp}((-\pi, x_2)^T; x^s), \quad x_2 \in \mathbb{R}, \quad (8d)$$

under the condition that G_α^{qp} propagates outwards at infinity. We remark that $G_\alpha^{qp}(x; x^s)$ is the quasi-periodic Green's function for the unperturbed background space. Compared to Eqs. (5), Eqs. (8) are much easier to solve numerically as now we only need to truncate the x_2 -direction. Once G_α^{qp} is obtained, we can evaluate G by directly applying the IFB transform to G_α^{qp} , and get,

$$G(x; x^s) = \int_{-1/2}^{1/2} G^{qp}(\alpha, x; x^s) d\alpha. \quad (9)$$

To accurately discretize the integral (9), we need to figure out the regularity of the integrand G^{qp} w.r.t. the FB parameter α . According to [18], the integrand G^{qp} has two types of singularities as α ranges over $(-1/2, 1/2]$. First, G^{qp} has a square-root singularity of the form $\sqrt{\kappa \pm \alpha}$ at $\alpha = \mp\kappa$, where $\kappa \in (-1/2, 1/2]$ is chosen such that $k - \kappa \in \mathbb{N}$. Throughout this paper, we shall use the negative real axis as the branch cut of the square-root function $\sqrt{\cdot}$ to ensure that its argument always lies in $[0, \pi)$. The singular integrand can be made smoother under a rescaling transformation [28], or even made analytic by simple changes of variables [31]. Second, G^{qp} may have a pole at $\alpha = \alpha_0$ for some $\alpha_0 \in (-1/2, 1/2]$, which corresponds to a guided mode of the problem (8). In this case, the real path can be deformed to a new path in the complex plane to bypass α_0 , ensuring the analyticity of the integrand [29]. Then, high-accuracy quadratures can be adopted to discretize the tailored integral.

For the scattering problem under consideration, it is seen from a numerical perspective that no guided modes exist, though theoretical justifications remain open. It suffices to treat the square-root singularity. Suppose $\kappa \notin \{0, 1/2\}$ first. In [31], the integration domain $(-1/2, 1/2)$ is divided into four sub-intervals, with an appropriate change of variable applied to each to remove the singularity. In fact, it is enough to divide it into two sub-intervals. Specifically,

$$G = \int_{-1/2}^{1/2} G^{qp}(\alpha) d\alpha = \int_{-\kappa}^{1-\kappa} G^{qp}(\alpha) d\alpha = \left(\int_{-\kappa}^{\kappa} + \int_{\kappa}^{1-\kappa} \right) G^{qp}(\alpha) d\alpha, \quad (10)$$

where the arguments x and x^s are omitted for brevity. For the first integral on the r.h.s, to eliminate the square-root singularities $\sqrt{\kappa \pm \alpha}$ at $\alpha = \mp\kappa$, we introduce the substitution $\alpha = \kappa \cos \theta$ and obtain

$$\int_{-\kappa}^{\kappa} G^{qp}(\alpha) d\alpha = \kappa \int_0^{\pi} G^{qp}(\kappa \cos \theta) \sin \theta d\theta. \quad (11)$$

For the second integral, we use $\alpha = \frac{(2\kappa-1)\cos\theta+1}{2}$ and get

$$\int_{\kappa}^{1-\kappa} G^{qp}(\alpha) d\alpha = \frac{1-2\kappa}{2} \int_0^{\pi} G^{qp}\left(\frac{(2\kappa-1)\cos\theta+1}{2}\right) \sin \theta d\theta. \quad (12)$$

For an even integer n , we adopt the $n/2$ -point Gauss-Legendre quadrature to discretize each integral in (11) and (12), and get

$$G \approx \sum_{i=1}^n G^{qp}(\alpha_i) w_i = \sum_{i=1}^n G_{\alpha_i}^{qp} w_i, \quad (13)$$

where w_i and α_i are the weights and the n distinct nodes in $(-\kappa, 1 - \kappa)$, respectively. We note that n does not have to be proportional to the wavenumber k , as α is confined to $(-1/2, 1/2]$. For $\kappa \in \{0, 1/2\}$, we do not need to split the integration domain, and the corresponding change of variable is similar.

3.2. A BIE formulation for Problem (8)

In this subsection, we present a BIE formulation for computing G_{α}^{qp} for $\alpha = \alpha_i$ as in (13). It follows a previous work [21] that computes quasi-periodic wavefields for incident plane waves. We note that (13) suggests that α can be close to $\pm\kappa$ or $1 - \kappa$, corresponding to the Rayleigh anomaly, making it challenging to use quasi-periodic fundamental solutions to compute G_{α}^{qp} [8]. The key step of [21] is to formulate an effective boundary condition that truncates the unbounded domain Ω_p^0 . Write $\Omega_{p,H}^0 := \Omega_p^0 \cap \{x : |x_2| \leq H\}$ for $H > |x_2^s|$. We shall frequently omit the source point x^s to write $G_{\alpha}^{qp}(x)$ for brevity.

Owing to its quasi-periodicity, G_{α}^{qp} admits the following Rayleigh expansions

$$G_{\alpha}^{qp}(x) = \sum_{l \in \mathbb{Z}} B_l^{\pm} e^{i(\alpha_l x_1 \pm \beta_l(x_2 - H))}, \quad \pm x_2 \geq H, \quad (14)$$

where $\alpha_l = \alpha + l$, $\beta_l = \sqrt{k_0^2 - \alpha_l^2}$, and

$$B_l^{\pm} = \frac{1}{2\pi} \int_{-\pi}^{\pi} G_{\alpha}^{qp}((x_1, \pm H)^T) e^{-i\alpha_l \tilde{x}_1} d\tilde{x}_1. \quad (15)$$

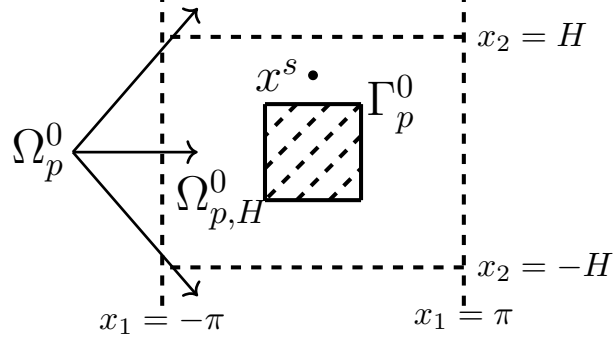


Figure 3: The periodic structure in the 0-th unit cell Ω_p^0 ; x^s represents a generic source point, TBCs (16) and (18) are established on $x_2 = \pm H$, and $\Omega_{p,H}^0$ denotes the truncated domain.

On $x_2 = H$, we get

$$\partial_{x_2} G_\alpha^{qp} \left(\begin{pmatrix} x_1 \\ H \end{pmatrix} \right) = \mathcal{B}_\alpha G_\alpha^{qp} \left(\begin{pmatrix} x_1 \\ H \end{pmatrix} \right), \quad (16)$$

where the Dirichlet-to-Neumann operator \mathcal{B}_α is defined as: for any α -quasiperiodic function $f \in C^\infty([- \pi, \pi])$,

$$(\mathcal{B}_\alpha f)(x) = \frac{i}{2\pi} \sum_{l=-\infty}^{\infty} \beta_l \left(\int_{-\pi}^{\pi} f(\tilde{x}) e^{-i\alpha_l \tilde{x}_1} d\tilde{x}_1 \right) e^{i\alpha_l x_1}. \quad (17)$$

It can be verified that $\mathcal{B}_\alpha e^{i\alpha_n x_1} = i\beta_n e^{i\alpha_n x_1}$ for all n . Similarly, on $x_2 = -H$,

$$\partial_{x_2} G_\alpha^{qp} \left(\begin{pmatrix} x_1 \\ -H \end{pmatrix} \right) = -\mathcal{B}_\alpha G_\alpha^{qp} \left(\begin{pmatrix} x_1 \\ -H \end{pmatrix} \right). \quad (18)$$

Equations (16) and (18) serve as TBCs for the unknown wavefield G_α^{qp} on $x_2 = \pm H$.

The scattered wave $G_\alpha^{sc}(x; x^s) := G_\alpha^{qp}(x; x^s) - \Phi(x; x^s)$ satisfies the homogeneous Helmholtz equation

$$\Delta G_\alpha^{sc} + k^2 G_\alpha^{sc} = 0, \quad \text{in } \Omega_{p,H}^0. \quad (19)$$

Thus, G^{sc} admits the following Green's representation formula

$$G_\alpha^{sc}(x) = \int_{\partial\Omega_{p,H}^0} [\Phi(x; y) \partial_\nu G_\alpha^{sc}(y) - \partial_\nu \Phi(x; y) G_\alpha^{sc}(y)] ds(y), \quad x \in \Omega_{p,H}^0, \quad (20)$$

where ν denotes the outer unit normal to the boundary $\partial\Omega_{p,H}^0$. As x approaches $\partial\Omega_{p,H}^0$, one obtains the following boundary integral equation [22]

$$(\mathcal{K} - \mathcal{K}_0[1])[G_\alpha^{sc}](x) = \mathcal{S}[\partial_\nu G_\alpha^{sc}](x), \quad (21)$$

for $x \in \partial\Omega_{p,H}^0$. Here, the boundary integral operators are defined as

$$\mathcal{S}[\phi](x) = 2 \int_{\partial\Omega_{p,H}^0} \Phi(x; y) \phi(y) ds(y), \quad (22)$$

$$\mathcal{K}[\phi](x) = 2 \text{P.V.} \int_{\partial\Omega_{p,H}^0} \partial_\nu \Phi(x; y) \phi(y) ds(y), \quad (23)$$

$$\mathcal{K}_0[\phi](x) = 2\text{P.V.} \int_{\partial\Omega_{p,H}^0} \partial_\nu \Phi_0(x; y) \phi(y) ds(y), \quad (24)$$

where $\Phi_0(x; y) = \frac{1}{2\pi} \log |x - y|$ is the fundamental solution of the two-dimensional Laplacian, and P.V. \int denotes the Cauchy principal integral. This induces a Neumann-to-Dirichlet (NtD) operator

$$\mathcal{N} = (\mathcal{K} - \mathcal{K}_0[1])^{-1} \mathcal{S}, \quad (25)$$

which maps $\partial_\nu G_\alpha^{sc}$ to G_α^{sc} on the boundary $\partial\Omega_{p,H}^0$.

We now formulate the problem in the form of abstract operators within the bounded rectangular domain $\Omega_{p,H}^0$. As shown in Figure 4, we denote the inner, left, bottom, right and top parts of $\partial\Omega_{p,H}^0$ as $\Gamma_{0,i}$ for $1 \leq i \leq 5$, respectively; note that $\Gamma_{0,1} = \Gamma_p^0$. Write $\psi_i = G_\alpha^{sc}|_{\Gamma_{0,i}}$, $\partial_\nu \psi_i = \partial_\nu G_\alpha^{sc}|_{\Gamma_{0,i}}$, $\Phi_i = \Phi|_{\Gamma_{0,i}}$, and $\partial_\nu \Phi_i = \partial_\nu \Phi|_{\Gamma_{0,i}}$. Thus,

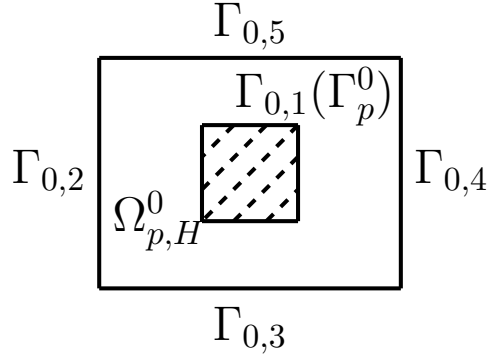


Figure 4: The inner, left, bottom, right and top parts $\Gamma_{0,j}$ for $j = 1, \dots, 5$.

$$\begin{bmatrix} \psi_1 \\ \psi_2 \\ \psi_3 \\ \psi_4 \\ \psi_5 \end{bmatrix} = \mathcal{N} \begin{bmatrix} \partial_\nu \psi_1 \\ \partial_\nu \psi_2 \\ \partial_\nu \psi_3 \\ \partial_\nu \psi_4 \\ \partial_\nu \psi_5 \end{bmatrix}, \quad (26)$$

On the other hand, the quasi-periodic conditions (8c) and (8d), the top and bottom conditions (16) and (18), and the Dirichlet condition (8b) lead to a matrix system

$$\mathcal{P}_\alpha \left(\begin{bmatrix} \psi_1 \\ \psi_2 \\ \psi_3 \\ \psi_4 \\ \psi_5 \end{bmatrix} + \begin{bmatrix} \Phi_1 \\ \Phi_2 \\ \Phi_3 \\ \Phi_4 \\ \Phi_5 \end{bmatrix} \right) = \mathcal{Q}_\alpha \left(\begin{bmatrix} \partial_\nu \psi_1 \\ \partial_\nu \psi_2 \\ \partial_\nu \psi_3 \\ \partial_\nu \psi_4 \\ \partial_\nu \psi_5 \end{bmatrix} + \begin{bmatrix} \partial_\nu \Phi_1 \\ \partial_\nu \Phi_2 \\ \partial_\nu \Phi_3 \\ \partial_\nu \Phi_4 \\ \partial_\nu \Phi_5 \end{bmatrix} \right), \quad (27)$$

where \mathcal{I} denotes the abstract identity operator, and

$$\mathcal{P}_\alpha = \begin{bmatrix} 0 & \mathcal{I} & 0 & -e^{2i\pi\alpha} \mathcal{I} & 0 \\ 0 & 0 & 0 & 0 & 0 \\ 0 & 0 & -\mathcal{B}_\alpha & 0 & 0 \\ 0 & 0 & 0 & 0 & \mathcal{B}_\alpha \\ \mathcal{I} & 0 & 0 & 0 & 0 \end{bmatrix}, \quad \mathcal{Q}_\alpha = \begin{bmatrix} 0 & 0 & 0 & 0 & 0 \\ 0 & \mathcal{I} & 0 & e^{2i\pi\alpha} \mathcal{I} & 0 \\ 0 & 0 & \mathcal{I} & 0 & 0 \\ 0 & 0 & 0 & 0 & \mathcal{I} \\ 0 & 0 & 0 & 0 & 0 \end{bmatrix}, \quad (28)$$

Combining (27) and (26),

$$(\mathcal{P}_\alpha \mathcal{N} - \mathcal{Q}_\alpha) \begin{bmatrix} \partial_\nu \psi_1 \\ \partial_\nu \psi_2 \\ \partial_\nu \psi_3 \\ \partial_\nu \psi_4 \\ \partial_\nu \psi_5 \end{bmatrix} = \mathcal{Q}_\alpha \begin{bmatrix} \partial_\nu \Phi_1 \\ \partial_\nu \Phi_2 \\ \partial_\nu \Phi_3 \\ \partial_\nu \Phi_4 \\ \partial_\nu \Phi_5 \end{bmatrix} - \mathcal{P}_\alpha \begin{bmatrix} \Phi_1 \\ \Phi_2 \\ \Phi_3 \\ \Phi_4 \\ \Phi_5 \end{bmatrix}. \quad (29)$$

On solving (29), we obtain $\partial_\nu G_\alpha^{sc}$ on $\partial\Omega_{p,H}^0$. Then, $G_\alpha^{sc} = \mathcal{N} \partial_\nu G_\alpha^{sc}$ on $\partial\Omega_{p,H}^0$. By Green's representation formula (20), G_α^{sc} and hence the total field $G_\alpha^{qp} = G_\alpha^{sc} + \Phi$ become available in $\Omega_{p,H}^0$. In the exterior region $\Omega_p^0 \setminus \overline{\Omega_{p,H}^0}$, we apply (15) to obtain the Rayleigh coefficients B_l^\pm first and then use (14) to evaluate G_α^{qp} . The following subsection is devoted to accurate approximations of \mathcal{N} and \mathcal{B}_α .

3.3. Numerical approximations of \mathcal{N} and \mathcal{B}_α

Following [22], we apply the Nyström method to discretize the three integral operators in (22)-(24). For completeness and for the later treatment of the TBC proposed in section 4.1, we present its brief idea below. We study the single-layer operator \mathcal{S} only; the other two operators are treated similarly.

As indicated in Figure 4, $\partial\Omega_{p,H}^0$ consists of two well-separated closed curves, a rectangle $\gamma_1 := \partial([-\pi, \pi] \times [-H, H]) = \bigcup_{j=2}^5 \Gamma_{0,j}$ and the obstacle boundary $\gamma_2 := \Gamma_{0,1}$. To simplify the presentation, we assume $x \in \gamma_1$ for the moment, and write

$$\begin{aligned} \mathcal{S}[\partial_\nu G_\alpha^{sc}](x) &= \int_{\gamma_1} \Phi(x; y) \partial_\nu G_\alpha^{sc}(y) ds(y) + \int_{\gamma_2} \Phi(x; y) \partial_\nu G_\alpha^{sc}(y) ds(y) \\ &:= \mathcal{S}^{(1)}[\partial_\nu G_\alpha^{sc}](x) + \mathcal{S}^{(2)}[\partial_\nu G_\alpha^{sc}](x). \end{aligned} \quad (30)$$

We consider the weakly singular operator $\mathcal{S}^{(1)}$ only.

Suppose γ_1 is parameterized by $x(s) = \{(x_1(s), x_2(s)) | 0 \leq s \leq L\}$ for the arc-length parameter s . Thus, we can parameterize $\mathcal{S}^{(1)}$ as

$$\mathcal{S}^{(1)}[\partial_\nu G_\alpha^{sc}](x(s)) = \int_0^L \Phi(x(s), x(s')) \partial_\nu G_\alpha^{sc}(x(s')) ds'. \quad (31)$$

We introduce a scaling function $s = \eta(t)$, $t \in [0, 2\pi]$ to smoothen the discontinuous density function $\partial_\nu G_\alpha^{sc}(x(s))$. Suppose $s_b = \eta(t_b)$ and $s_e = \eta(t_e)$ correspond to two consecutive corners with $0 \leq t_b < t_e \leq 2\pi$ and $0 \leq s_b < s_e \leq L$. We define [10, Eq. (3.104)]

$$\eta(t) = \frac{s_b \eta_1^p + s_e \eta_2^p}{\eta_1^p + \eta_2^p}, \quad t \in [t_b, t_e], \quad (32)$$

where p is a positive integer, and

$$\eta_1 = \left(\frac{1}{2} - \frac{1}{p}\right)\xi^3 + \frac{\xi}{p} + \frac{1}{2}, \quad \eta_2 = 1 - \eta_1, \quad \xi = \frac{2t - (t_b + t_e)}{t_e - t_b}. \quad (33)$$

Using a uniform mesh of N points $\{t_j = 2\pi j/N\}_{j=0}^{N-1}$ on $[0, 2\pi]$ for an even integer $N > 0$, $s_j = \eta(t_j)$ generates a graded mesh with grid points clustering near corners and uniformly spaced away from them; in our implementation, corners are chosen as part of the grid points and the mesh points on $\Gamma_{0,4}$ should be the translate of those on $\Gamma_{0,2}$. To simplify the notation, we use $x(t)$ and $x'(t)$ to denote $x(\eta(t))$ and $x'(\eta(t))\eta'(t)$, respectively.

Now, equation (31) becomes

$$\mathcal{S}^{(1)}[\partial_\nu G_\alpha^{sc}](x(t)) = \int_0^{2\pi} S(t, \tau) \phi_\alpha^{sc}(\tau) d\tau, \quad (34)$$

where $\phi_\alpha^{sc}(\tau) = \partial_\nu G_\alpha^{sc}(\tau)\eta'(\tau)$ and $S(t, \tau) := \frac{i}{2}H_0^{(1)}(k|x(t) - x(\tau)|)$; here we use the scaled normal derivative ϕ_α^{sc} in place of $\partial_\nu G_\alpha^{sc}$ because it can significantly reduce the condition number of the approximate matrix of $S^{(1)}$ given below [20]. The kernel function S can be split as [10]

$$S(t, \tau) = S_1(t, \tau) \ln(4 \sin^2 \frac{t - \tau}{2}) + S_2(t, \tau), \quad (35)$$

where

$$S_1(t, \tau) = -\frac{1}{2\pi} J_0(k|x(t) - x(\tau)|), \quad (36)$$

$$S_2(t, \tau) = \begin{cases} S(t, \tau) - S_1(t, \tau) \ln(4 \sin^2 \frac{t - \tau}{2}), & t \neq \tau, \\ \frac{i}{2} - \frac{C}{\pi} - \frac{1}{\pi} \ln\left(\frac{k}{2}|x'(t)|\right), & t = \tau, \end{cases} \quad (37)$$

and C denotes Euler's constant. Then, we approximate

$$S^{(1)}[\partial_\nu G_\alpha^{sc}](x(t_j)) \approx \sum_{k=0}^{N-1} [R_{|k-j|}^{(N)} S_1(t_j, t_k) + \frac{2\pi}{N} S_2(t_j, t_k)] \phi_\alpha^s(t_k), \quad j = 0, \dots, N-1, \quad (38)$$

where

$$R_n^{(N)} := -\frac{4\pi}{N} \sum_{m=1}^{N/2} \frac{1}{m} \cos \frac{2mn\pi}{N} - \frac{4\pi}{N^2} (-1)^n.$$

This gives rise to

$$S^{(1)}[\partial_\nu G_\alpha^{sc}] \begin{bmatrix} x(t_0) \\ x(t_1) \\ \vdots \\ x(t_{N-1}) \end{bmatrix} = \mathbf{S}_{11} \begin{bmatrix} \phi_\alpha^s(t_0) \\ \phi_\alpha^s(t_1) \\ \vdots \\ \phi_\alpha^s(t_{N-1}) \end{bmatrix}, \quad (39)$$

for an $N \times N$ matrix \mathbf{S}_{11} , where the l.h.s. represents a column vector of elements $S^{(1)}[\partial_\nu G_\alpha^{sc}](x(t_j))$.

To discretize $S^{(2)}[\partial_\nu G_\alpha^{sc}](x(t_j))$, we can use the same approach, in fact simpler due to $x(t_j) \notin \gamma_2$, to obtain an $N \times M$ matrix \mathbf{S}_{12} , where M is the number of grid points on γ_2 . Note that the M grid points are uniformly spaced in the parameter space when γ_2 is smooth, and form a graded mesh otherwise. Now consider (30) for $x \in \gamma_2$. Using the same grid points on Γ_0 , we can obtain an $M \times N$ matrix \mathbf{S}_{21} for the operator $S^{(1)}$ and an $M \times M$ matrix \mathbf{S}_{22} for the operator $S^{(2)}$. Consequently, the matrix $\mathbf{S} = [\mathbf{S}_{ij}]_{i,j=1,2}$ represents an accurate approximation of the single-layer operator S on $\gamma_1 \cup \gamma_2$.

Applying a similar procedure to \mathcal{K} and \mathcal{K}_0 as above, (21) can be approximated by

$$(\mathbf{K} - \mathbf{D}) \mathbf{G}_\alpha^{sc} = \mathbf{S} \phi_\alpha^{sc}, \quad (40)$$

where \mathbf{K} is an $(M + N) \times (M + N)$ matrix approximating \mathcal{K} , \mathbf{D} is a diagonal matrix with diagonal elements approximating $\mathcal{K}_0[1]$, and $\mathbf{G}_\alpha^{sc}(\phi_\alpha^{sc})$ represents a column vector of $G_\alpha^{sc}(\phi_\alpha^{sc})$ at the $M + N$ grid points on $\gamma_1 \cup \gamma_2$. This gives rise to an $(M + N) \times (M + N)$ matrix

$$\mathbf{N} = (\mathbf{K} - \mathbf{D})^{-1} \mathbf{S}, \quad (41)$$

approximating the NtD operator \mathcal{N} .

Now, suppose the top segment of γ_1 , namely $\Gamma_{0,5}$, is parameterized in t as $x(t)$ for $0 \leq t \leq T$, and the graded mesh points on it are $\{t_k\}_{k=0}^{N_0-1}$ for some integer $N_0 > 0$. For the top boundary condition (16), we can apply the trapezoidal rule to the integrals in (17) and get [21]

$$\phi_\alpha^{qp}(x(t_j)) := \eta'(t_j) \partial_\nu G_\alpha^{qp}(x(t_j)) = \eta'(t_j) (\mathcal{B}_\alpha G_\alpha^{qp})(x(t_j))$$

$$\begin{aligned} & \approx \frac{\mathbf{i}}{2\pi} \sum_{l=-J_0}^{J_0} \eta'(t_j) \beta_l e^{i\alpha_l x_1(t_j)} \int_0^T G_\alpha^{qp}(x(\tau)) e^{-i\alpha_l x_1(\tau)} \eta'(\tau) d\tau \\ & \approx \sum_{k=0}^{N_0-1} \left[\frac{iT\eta'(t_j)}{2\pi N_0} \sum_{l=-J_0}^{J_0} \beta_l e^{i\alpha_l x_1(t_j)} e^{-i\alpha_l x_1(t_k)} \eta'(t_k) \right] G_\alpha^{qp}(x(t_k)), \end{aligned}$$

for $0 \leq j \leq N_0 - 1$. Since the Rayleigh coefficients B_l decay exponentially with l , a moderately large integer J_0 ensures sufficient accuracy in practice. The bracketed coefficients can be rapidly evaluated via the nonuniform fast Fourier transform, and form an $N_0 \times N_0$ matrix \mathbf{B}_α such that

$$\boldsymbol{\phi}_\alpha^{qp} = \mathbf{B}_\alpha \mathbf{G}_\alpha^{qp}, \quad (42)$$

where $\boldsymbol{\phi}_\alpha^{qp}$ is a column vector of the N_0 elements $\phi_\alpha^{qp}(x(t_j))$, etc. Roughly speaking, \mathbf{B}_α can be regarded as an approximation of the scaled operator $\eta' \mathcal{B}_\alpha$.

3.4. Evaluating Green's function and its derivatives

With the two approximate matrices \mathbf{N} and \mathbf{B}_α , we are ready to evaluate the Green's function $G(x; x^s)$ and its derivatives in all cells Ω_p^j , which are the key ingredients in solving the original scattering problem (1)-(4). Let $\Omega_{p,H}^j := \Omega_p^j \cap \{x : |x_2| \leq H\}$ and $\partial\Omega_{p,H}^j$ be its boundary for any $j \in \mathbb{Z}$.

We first discuss the Green's function G in Ω_p^0 . Equation (29) can be approximated by the following linear system

$$\mathbf{A}(\alpha) \boldsymbol{\phi}_\alpha^{sc}(x^s) = \mathbf{b}(\alpha; x^s), \quad (43)$$

where the $(M+N) \times (M+N)$ matrix \mathbf{A} is related to the operator $\mathcal{P}_\alpha \mathcal{N} - \mathcal{Q}_\alpha$ and the nonzero $(M+N) \times 1$ column vector \mathbf{b} approximates the r.h.s. of (29). Note that we have multiplied the third and fourth row of (29) with w' to before establishing (43). Solving the linear system, we get $\boldsymbol{\phi}_\alpha^{sc}$ and then $\mathbf{G}_\alpha^{sc} = \mathbf{N} \boldsymbol{\phi}_\alpha^{sc}$ on the boundary $\partial\Omega_{p,H}^0$.

For any observation point $x \in \Omega_{p,H}^0$, using the trapezoidal rule with the mesh points on the boundary $\partial\Omega_{p,H}^0$ as the nodes to discretize the integrals in the two representation formulae (20), we can evaluate $G_\alpha^{sc}(x; x^s)$ from $\boldsymbol{\phi}_\alpha^{sc}$ and \mathbf{G}_α^{sc} . With the IFB transform (10) and the quadrature (13), we can evaluate the background Green's function $G(x; x^s)$ and its gradient $\nabla_x G(x; x^s)$ for any $x \in \Omega_{p,H}^0$. The above procedure can be simply understood as numerical approximations of

$$\begin{aligned} G(x; x^s) &= \Phi(x; x^s) \\ &+ \int_{-\kappa}^{1-\kappa} d\alpha \int_{\partial\Omega_{0,H}^0} [\Phi(x; z) \partial_{\nu(z)} G_\alpha^{sc}(z; x^s) - \partial_{\nu(z)} \Phi(x; z) G_\alpha^{sc}(z; x^s)] ds(z), \end{aligned} \quad (44)$$

and its x -gradient. Suppose we need to evaluate G at N_o observation points $\{x_j^o\}_{j=1}^{N_o}$ in $\Omega_{p,H}^0$ for the fixed source point x^s . As $\partial\Omega_{p,H}^0$ is discretized by $M+N$ points and the interval $(-\kappa, 1-\kappa)$ by n points, it is not hard to find that the computational complexity above is $\mathcal{O}(N_o n(M+N))$. If we further require G at N_s source points $\{x_k^s\}_{k=1}^{N_s}$, then the complexity becomes $\mathcal{O}(N_o N_s n(M+N))$, which is too costly. Nevertheless, by interchanging the order of integrations in (44),

$$\begin{aligned} G(x; x^s) &= \Phi(x; x^s) + \int_{\partial\Omega_{0,H}^0} \left[\Phi(x; z) \int_{-\kappa}^{1-\kappa} \partial_{\nu(z)} G_\alpha^{sc}(z; x^s) d\alpha \right. \\ &\quad \left. - \partial_{\nu(z)} \Phi(x; z) \int_{-\kappa}^{1-\kappa} G_\alpha^{sc}(z; x^s) d\alpha \right] ds(z) \\ &= \Phi(x; x^s) + \int_{\partial\Omega_{0,H}^0} [\Phi(x; z) \partial_{\nu(z)} G^{sc}(z; x^s) - \partial_{\nu(z)} \Phi(x; z) G^{sc}(z; x^s)] ds(z). \end{aligned} \quad (45)$$

Eq. (45) evaluates $\partial_{v(z)} G^{sc}(z; x^s)$ and $G^{sc}(z; x^s)$ for $z \in \partial\Omega_{p,H}^0$ first, significantly reducing the complexity to $\mathcal{O}((N_o + n)N_s(M + N))$. This makes the numerical evaluations almost n times faster!

According to (8) and $\nabla_{x^s} G_\alpha^{sc}(x; x^s) = \nabla_{x^s} G_\alpha^{qp}(x; x^s) - \nabla_{x^s} \Phi(x; x^s)$, by replacing G_α^{qp} by $\nabla_{x^s} G_\alpha^{qp}$ and the r.h.s. of (8a) by $-\nabla_{x^s} \delta(x - x^s)$, we can evaluate $\nabla_{x^s} G_\alpha^{qp}$ by the same method in Section 3.2. As for $x \in \Omega_p^0 \setminus \overline{\Omega_{p,H}^0}$, we use G_α^{qp} on $x_2 = \pm H$ to get the Rayleigh coefficients by (15) and then (14) to compute G_α^{qp} and its derivatives. The IFB transform (13) then applies to compute G and its derivatives in $\Omega_p^0 \setminus \overline{\Omega_{p,H}^0}$; we omit the details here. The above procedure is summarized in Algorithm 1 below.

Algorithm 1 Evaluating the Green's function and its gradient in Ω_p^0 .

Require: n quadrature nodes $\{\alpha_i\}_{i=1}^n \subset (-\kappa, 1 - \kappa)$; $M + N$ mesh points $\{x_l\}_{l=1}^{M+N} \subset \partial\Omega_{p,H}^0$; N_o observation points $\{x_j^o\}_{j=1}^{N_o} \subset \Omega_{p,H}^0$; N_s source points $\{x_k^s\}_{k=1}^{N_s} \subset \Omega_{p,H}^0$.

- 1: Approximate the operator \mathcal{N} by \mathbf{N} as in (41), and the operator \mathcal{B}_{α_i} by \mathbf{B}_{α_i} as in (42) for $\alpha = \alpha_i$;
- 2: **for** $i = 1; i < n; i++$ **do**
- 3: Solve the linear system $\mathbf{A}(\alpha_i) \boldsymbol{\phi}_{\alpha_i}^{sc}(x_k^s) = \mathbf{b}(\alpha_i; x_k^s)$ according to (43) for $\boldsymbol{\phi}_{\alpha_i}^{sc}(x_k^s)$ on $\partial\Omega_{p,H}^0$;
- 4: **end for**
- 5: Evaluate $G^{sc}(x_l; x_k^s)$, $\partial_v G^{sc}(x_l; x_k^s)$ and their gradients w.r.t x^s by (13);
- 6: Evaluate $G(x_j^o; x_k^s)$ and $\nabla_{x^s} G(x_j^o; x_k^s)$ via (45);
- 7: Evaluate $G(x; x_k^s)$ and $\nabla_{x^s} G(x; x_k^s)$ by (14) and then (13) for any $x \in \Omega_p^0 \setminus \overline{\Omega_{p,H}^0}$.

As $\mathbf{A}(\alpha_i)$ depends on α_i only, we can compute the LU decomposition of $\mathbf{A}(\alpha_i)$ just once for all source points x_k^s . Thus, the computational complexity for solving the nN_s linear systems becomes $\mathcal{O}((M + N)^2 n(M + N + N_s))$. In summary, the computational complexity of Algorithm 1 for Steps 1 through 6 is

$$\mathcal{O}((M + N)^3) + \mathcal{O}((M + N)^2 n(M + N + N_s)) + \mathcal{O}(N_o N_s n(M + N)),$$

where the first term accounts for computing \mathbf{N} , the second for the nN_s linear systems, and the last for evaluating G and its gradient. In practice, the prefactor of the first term is much larger than the second term, making it the most costly to approximate the NTD map \mathcal{N} during the whole procedure. In other words, the speed of Algorithm 1 for evaluating the background Green's function G will not be significantly slower than that for the simpler quasi-periodic Green's function G_α^{qp} , as both require approximating \mathcal{N} !

Algorithm 2 Evaluating the Green's function and its gradient in Ω_p^j for $j \neq 0$.

Require: $M + N$ mesh points $\{x_l\}_{l=1}^{M+N}$ on $\partial\Omega_{p,H}^0$; $M + N$ mesh points $\{x_l^{(j)}\}_{l=1}^{M+N}$ on $\partial\Omega_{p,H}^j$; N_s source points $\{x_k^s\}_{k=1}^{N_s} \subset \Omega_{p,H}^0$.

- 1: Compute $\boldsymbol{\phi}_{\alpha_i}^{sc}(x_k^s)$, $G_{\alpha_i}^{sc}(x_k^s)$ and their gradients w.r.t x^s on $\partial\Omega_{p,H}^0$ by Algorithm 1;
- 2: Compute $\boldsymbol{\phi}_{\alpha_i}^{sc,(j)}(x_k^s)$, $G_{\alpha_i}^{sc,(j)}(x_k^s)$ and their gradients w.r.t x^s on $\partial\Omega_{p,H}^j$ by (7);
- 3: Evaluate $G^{sc}(x_l^{(j)}; x_k^s)$, $\partial_v G^{sc}(x_l^{(j)}; x_k^s)$ and their gradients w.r.t x^s by (13);
- 4: Obtain $G(x_l^{(j)}; x_k^s) = \Phi(x_l^{(j)}; x_k^s) + G^{sc}(x_l^{(j)}; x_k^s)$ and $\nabla_{x^s} G(x_l^{(j)}; x_k^s) = \nabla_{x^s} \Phi(x_l^{(j)}; x_k^s) + \nabla_{x^s} G^{sc}(x_l^{(j)}; x_k^s)$;
- 5: Evaluate $G(x; x_k^s)$ and $\nabla_{x^s} G(x; x_k^s)$ via (45) for any $x \in \Omega_{p,H}^j$;
- 6: Evaluate $G(x; x_k^s)$ and $\nabla_{x^s} G(x; x_k^s)$ by (14) and then (13) for any $x \in \Omega_p^j \setminus \overline{\Omega_{p,H}^j}$.

Next, we use the quasi-periodicity of G_α^{pq} to compute the background Green's function G in any other cell Ω_p^j for $j \neq 0$ and for the same set of sources $\{x_k^s\} \subset \Omega_{p,H}^0$. As in Algorithm 1, we first evaluate G on the boundary $\partial\Omega_{p,H}^j$. To discretize $\partial\Omega_{p,H}^j$, we horizontally translate the $(M + N)$ mesh points $\{x_l\}_{l=1}^{M+N} \subset \partial\Omega_{p,H}^0$ by j periods, denoted by

$\{x_l^{(j)}\}_{l=1}^{M+N}$. Then, $\mathbf{G}_\alpha^{pq,(j)}$ and $\boldsymbol{\phi}_\alpha^{pq,(j)}$, the vectors of G_α^{pq} and ϕ_α^{pq} at $x_l^{(j)}$, satisfy

$$\mathbf{G}_\alpha^{pq,(j)} = e^{i2\pi\alpha j} \mathbf{G}_\alpha^{pq}, \quad \boldsymbol{\phi}_\alpha^{pq,(j)} = e^{i2\pi\alpha j} \boldsymbol{\phi}_\alpha^{pq}.$$

Applying the inverse Floquet-Bloch transform (13), we obtain G^{pq} and hence G on $\partial\Omega_{p,H}^j$. Then, similar to steps 6 and 7 in Algorithm 1, we can obtain G and its derivatives in Ω_p^j . The above procedure is summarized in Algorithm 2.

4. The original scattering problem

With the background Green's function G available, we are ready to solve the original scattering problem (2)-(4) now. First, we construct a TBC in the perturbed region Ω_{np}^0 to truncate the unbounded domain Ω_{np} .

4.1. Transparent boundary condition

Let $\tilde{\Gamma}$ be an artificial curve that encloses both the perturbation and the original unperturbed obstacle in the same cell. For simplicity, we choose $\tilde{\Gamma}$ to be analytic and sufficiently away from the obstacles, as indicated in Figure 5. As

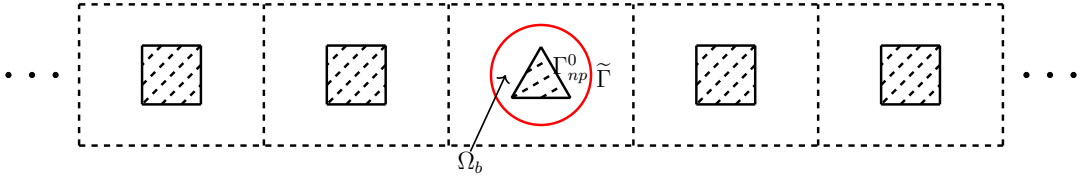


Figure 5: The artificial curve $\tilde{\Gamma}$ and the perturbed region Ω_b .

we have assumed that both u^{og} and G satisfy the SRC condition (3), we may follow the arguments in [10, Therorem 2.5] to derive the following BIE for u^{og} on $\tilde{\Gamma}$,

$$(\tilde{\mathcal{K}} - \mathcal{I})u^{\text{og}} = \tilde{\mathcal{S}}\partial_\nu u^{\text{og}}, \quad (46)$$

where the single-layer and double-layer operators $\tilde{\mathcal{S}}$ and $\tilde{\mathcal{K}}$ are now defined with the background Green's function G in place of the fundamental solution Φ ,

$$\tilde{\mathcal{S}}[\phi](x) = 2 \int_{\tilde{\Gamma}} G(x; y) \phi(y) ds(y), \quad (47)$$

$$\tilde{\mathcal{K}}[\phi](x) = 2\text{P.V.} \int_{\tilde{\Gamma}} \partial_{\nu(y)} G(x; y) \phi(y) ds(y). \quad (48)$$

The new BIE (46) serve as a TBC to truncate the unbounded domain, and can be discretized by using the same Nyström method in section 3.3, but with a rather simple procedure. We note that the adjoint double-layer and hypersingular operators can also be incorporated here to possibly construct a better-conditioned TBC numerically based on direct or indirect formulations [10].

Take $\tilde{\mathcal{S}}$ as an example. It satisfies

$$\tilde{\mathcal{S}}[\phi](x) = 2 \int_{\tilde{\Gamma}} \Phi(x; y) \phi(y) ds(y) + 2 \int_{\tilde{\Gamma}} G^{sc}(x; y) \phi(y) ds(y). \quad (49)$$

As $\tilde{\Gamma}$ is smooth, we can apply the same kernel splitting method in section 3.3 to discretize the first term without using any scaling function. To discretize the second term, we directly apply the trapezoidal rule as the integrand is analytic. One similarly discretizes $\tilde{\mathcal{K}}$.

Suppose $\tilde{\Gamma}$ is discretized by $N_p > 0$ grid points, forming the set $\tilde{\Gamma}_{\text{num}}$. The above discretizing procedure requires evaluating the analytic part $G^{sc}(x; y)$ and its gradient $\nabla_y G^{sc}(x; y)$ for any $x, y \in \tilde{\Gamma}_{\text{num}}$. This can be done by taking $N_o = N_s = N_p$ and choosing $x_j^o, x_k^s \in \tilde{\Gamma}_{\text{num}}$ in Algorithm 3.1. Thus, we obtain two $N_p \times N_p$ matrices $\tilde{\mathbf{S}}$ and

$\tilde{\mathbf{K}}$ approximating the two operators $\tilde{\mathcal{S}}$ and $\tilde{\mathcal{K}}$, respectively. Consequently, (46) gives rise to an $N_p \times N_p$ matrix $\tilde{\mathbf{N}} = (\tilde{\mathbf{K}} - \mathbf{I})^{-1} \tilde{\mathbf{S}}$ such that

$$\mathbf{u}^{\text{og}} \approx \tilde{\mathbf{N}} \boldsymbol{\phi}^{\text{og}}, \quad (50)$$

where \mathbf{u}^{og} and $\boldsymbol{\phi}^{\text{og}}$ are column vectors of u^{og} and $\partial_v u^{\text{og}}$ at the N_p grid points. Thus, $\tilde{\mathbf{N}}$ can be regarded as an approximation of the NtD operator $\tilde{\mathcal{N}} = (\tilde{\mathcal{K}} - \mathbf{I})^{-1} \tilde{\mathcal{S}}$. Based on the NtD operator $\tilde{\mathcal{N}}$ and its approximation $\tilde{\mathbf{N}}$, we numerically solve the original problem for the two incidences in the following two sections.

4.2. Wavefield in the perturbed region

As shown in Figure 5, let Γ_{np}^0 be the boundary of the deformed obstacle, and Ω_b be the domain bounded by $\tilde{\Gamma}$ and Γ_{np} . We compute u^{tot} in the perturbed region Ω_b in this subsection.

We study the cylindrical incidence first. Suppose the source point $x^* \in \Omega_b$; the case $x^* \notin \Omega_b$ will be discussed in Remark 4.2. As $u^{\text{og}}(x) = u^{\text{tot}}(x; x^*)$ satisfies the SRC condition (3), equation (50) implies

$$\mathbf{u}_1^{\text{tot}} = \tilde{\mathbf{N}} \boldsymbol{\phi}_1^{\text{tot}}, \quad (51)$$

or equivalently

$$\mathbf{u}_1^{\text{sc}} + \mathbf{u}_1^{\text{inc}} = \tilde{\mathbf{N}}(\boldsymbol{\phi}_1^{\text{s}} + \boldsymbol{\phi}_1^{\text{inc}}), \quad (52)$$

where \mathbf{u}_1^{sc} denotes the vector of u^{sc} at the N_p grid points on $\tilde{\Gamma}$, etc. In Ω_b , $u^{\text{sc}} = u^{\text{tot}} - u^{\text{inc}}$ satisfies the homogeneous Helmholtz equation. Applying the same BIE approach presented in section 3.3, we obtain an NtD matrix $\hat{\mathbf{N}}$ that satisfies

$$\begin{bmatrix} \mathbf{u}_1^{\text{sc}} \\ \mathbf{u}_2^{\text{sc}} \end{bmatrix} = \hat{\mathbf{N}} \begin{bmatrix} \boldsymbol{\phi}_1^{\text{sc}} \\ \boldsymbol{\phi}_2^{\text{sc}} \end{bmatrix}, \quad (53)$$

where \mathbf{u}_j^{sc} and $\boldsymbol{\phi}_j^{\text{sc}}$ represent column vectors of u^{sc} and $\partial_v u^{\text{sc}}$ at the grid points on $\tilde{\Gamma}$ and Γ_{np}^0 , respectively. Note that we have used the same set of grid points as in (50) and $\boldsymbol{\phi}_2^{\text{sc}}$ should approximate a scaled normal derivative, the product of $\partial_v u^{\text{sc}}$ and a scaling function analogous to w in (32), if Γ_{np}^0 contains corners. Besides, the boundary condition on Γ_{np}^0 implies

$$\mathbf{u}_2^{\text{inc}} + \mathbf{u}_2^{\text{sc}} = 0. \quad (54)$$

Solving the linear system (52)-(54), we obtain the unknowns \mathbf{u}_j^{sc} and $\boldsymbol{\phi}_j^{\text{sc}}$. Based on Green's representation formula, analogous to (20) but with $\partial\Omega_{p,H}^0$ replaced by $\partial\Omega_b$, the boundary of Ω_b , we can apply the trapezoidal rule to obtain $u^{\text{sc}}(x)$ for any $x \in \Omega_b$ by directly using the grid points on $\partial\Omega_b$. Then, the total wavefield $u^{\text{tot}}(x; x^*) = u^{\text{sc}}(x; x^*) + \Phi(x; x^*)$ becomes available in Ω_b .

For the plane-wave incidence $u^{\text{inc}} = e^{ik(\cos \theta x_1 - \sin \theta x_2)}$, we follow closely the procedures in sections 3.2 and 3.3 to compute the quasi-periodic reference wavefield $u_{\text{ref}}^{\text{tot}}$; see also [21]. Then, (52) should be changed to

$$\mathbf{u}_1^{\text{tot}} - \mathbf{u}_{\text{ref},1}^{\text{tot}} = \tilde{\mathbf{N}}(\boldsymbol{\phi}_1^{\text{tot}} - \boldsymbol{\phi}_{\text{ref},1}^{\text{tot}}), \quad (55)$$

where $\mathbf{u}_{\text{ref},1}^{\text{tot}}$ denotes the vector of $u_{\text{ref}}^{\text{tot}}$ at the N_p grid points on $\tilde{\Gamma}$. Equation (53) still holds but with u^{sc} replaced by u^{tot} . Equation (54) now becomes $\mathbf{u}_2^{\text{tot}} = 0$. Solving the new linear system, we obtain $\mathbf{u}_j^{\text{tot}}$ and $\boldsymbol{\phi}_j^{\text{tot}}$ on $\partial\Omega_b$. Green's representation formula then applies to get u^{tot} in Ω_b .

The above procedure is summarized in Algorithm 3.

4.3. Wavefield in the unperturbed region

In this section, we shall make use of Algorithms 1 and 2 to compute the wavefield outside Ω_b . To simplify the presentation, we discuss the cylindrical incidence only; the case for the plane-wave incidence can be analyzed similarly.

The algorithm can basically be divided into two procedures: (1) Leap; (2) Pullback, as illustrated in Figure 6. In the leap procedure, we make use of the total wavefield u^{tot} on the artificial boundary $\tilde{\Gamma}$ to get u^{tot} on the boundary $\partial\Omega_{np,H}^j$.

Algorithm 3 Computing the wavefield u^{tot} in Ω_b .

Require: N_p discretization points $\{x_k^s\}_{k=1}^{N_p}$ on $\tilde{\Gamma}$;

- 1: Compute $G^{sc}(x_{k'}^{s'}; x_k^s)$ and $\nabla_{x^s} G^{sc}(x_{k'}^{s'}; x_k^s)$ by Steps 1 through 5 of Algorithm 1 for any $1 \leq k', k \leq N_p$;
- 2: Approximate the NtD operator $\tilde{\mathcal{N}}$ by the $N_p \times N_p$ matrix $\tilde{\mathbf{N}}$ for the exterior domain $\Omega_{np} \setminus \overline{\Omega_b} = \Omega_p \setminus \overline{\Omega_b}$, and establish the TBC equation (50);
- 3: Use the BIE approach in section 3.3 to obtain the NtD matrix $\hat{\mathbf{N}}$ in (53) for the interior domain Ω_b ;
- 4: Solve equations (52)-(54) for \mathbf{u}_j^{sc} and $\boldsymbol{\phi}_j^{\text{sc}}$ for $j = 1, 2$ on $\tilde{\Gamma} \cup \Gamma_{np}^0$;
- 5: For any $x \in \Omega_b$, evaluate $u^{\text{sc}}(x)$ by using the trapezoidal rule to discretize

$$u^{\text{tot}}(x) = u^{\text{inc}}(x) + \int_{\partial\Omega_b} [\partial_{v(y)} \Phi(x; y) u^{\text{sc}}(y) - \Phi(x; y) \partial_v u^{\text{sc}}(y)] ds(y),$$

in terms of \mathbf{u}_j^{sc} and $\boldsymbol{\phi}_j^{\text{sc}}$ for $j = 1, 2$;

of the j -th cell, called the leap procedure \mathcal{L}_j . In the pullback procedure, we make use of u^{tot} on $\partial\Omega_{np,H}^j$ to compute u^{tot} in the j -th unit cell Ω_{np}^j , called the pullback procedure \mathcal{P} .

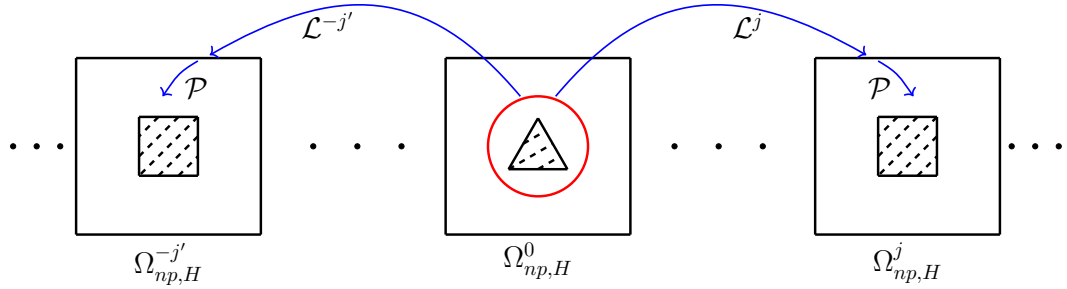


Figure 6: The leap procedures \mathcal{L}^j and $\mathcal{L}^{-j'}$, and the pullback procedure \mathcal{P} .

We discuss $j \neq 0$ first so that $\Omega_{np}^j = \Omega_p^j$. To evaluate u^{tot} in Ω_p^j , we need to compute $u^{\text{tot}}(x)$ and the normal derivative $\partial_v u^{\text{tot}}(x)$ for $x \in \partial\Omega_{p,H}^j$ first; note that $u^{\text{tot}} = 0$ on the obstacle boundary Γ_p^j . As we have obtained u^{tot} and $\partial_v u^{\text{tot}}$ on $\tilde{\Gamma}$, we directly adopt the following Green's representation formula

$$u^{\text{tot}}(x) = \int_{\tilde{\Gamma}} [\partial_{v(y)} G(x; y) u^{\text{tot}}(y) - G(x; y) \partial_{v(y)} u^{\text{tot}}(y)] ds(y), \quad (56)$$

to evaluate $u^{\text{tot}}(x)$ for $x \in \partial\Omega_{p,H}^j$. In doing so, we use the trapezoidal rule to discretize the above integral by using $\tilde{\Gamma}_{\text{num}}$ as the set of grid points on $\tilde{\Gamma}$ and then apply Algorithm 3.1 to evaluate $\partial_{v(y)} G(x; y)$ and $G(x; y)$ for $y \in \tilde{\Gamma}_{\text{num}}$ and $x \in \partial\Omega_{p,H}^j$. We can directly take the gradient of (56) w.r.t. x to evaluate ∇u^{tot} and hence $\partial_v u^{\text{tot}}$ on $\partial\Omega_{p,H}^j$ as well. Next, Green's representation formula, using Φ instead of G , applies to get u^{tot} everywhere in Ω_p^j . As for $u^{\text{tot}}(x)$ for any $x \in \Omega_p^j \cap \{x : |x_2| \geq H\}$, we can use step 6 of Algorithm 2 to evaluate $G(x; y)$ and its derivatives for $y \in \tilde{\Gamma}_{\text{num}}$, and then use (56) to compute $u^{\text{tot}}(x)$. As for $j = 0$, we only need to replace $\partial\Omega_{p,H}^j$ above by the rectangular boundary $\partial((-\pi, \pi) \times (-H, H))$. We put all details together in Algorithm 4 below.

Algorithm 4 Computing the wavefield in $\Omega_{np}^j \setminus \overline{\Omega_b}$ for any $j \in \mathbb{Z}$.

Require: N mesh points $\{x_l^{(j)}\}_{l=1}^N$ on $\partial\Omega_{np,H}^j$; N_p mesh points $\{x_k^s\}_{k=1}^{N_p}$ on $\tilde{\Gamma}$; $u^{\text{tot}}(x_k^s)$ and $\partial_\nu u^{\text{tot}}(x_k^s)$ on $\tilde{\Gamma}$ computed in section 4.2.

1: Compute $G(x_l^{(j)}; x_k^s)$ and $\nabla_{x^s} G(x_l^{(j)}; x_k^s)$ by Steps 1 through 4 of Algorithm 2;

2: Leap \mathcal{L}_j : evaluate $u^{\text{tot}}(x_l^{(j)})$ and $\partial_\nu u^{\text{tot}}(x_l^{(j)})$ on $\partial\Omega_{np,H}^j \setminus \overline{\Omega_b}$ by using the trapezoidal rule, with the set of nodes $\tilde{\Gamma}_{\text{num}}$, to discretize

$$\partial_{x_1}^{j_1} \partial_{x_2}^{j_2} u^{\text{tot}}(x) = \partial_{x_1}^{j_1} \partial_{x_2}^{j_2} \int_{\tilde{\Gamma}} [\partial_{\nu(y)} G(x; y) u^{\text{tot}}(y) - G(x; y) \partial_\nu u^{\text{tot}}(y)] ds(y),$$

for $0 \leq j_1 + j_2 \leq 1$.

3: Pullback \mathcal{P} : for any $x \in \Omega_{np,H}^j \setminus \overline{\Omega_b}$, evaluate $u^{\text{tot}}(x)$ by using the trapezoidal rule to discretize

$$u^{\text{tot}}(x) = \int_{\partial(\Omega_{np,H}^j \setminus \overline{\Omega_b})} [\partial_{\nu(y)} \Phi(x; y) u^{\text{tot}}(y) - \Phi(x; y) \partial_\nu u^{\text{tot}}(y)] ds(y).$$

4: For any $x \in \Omega_{np}^j \setminus \overline{\Omega_{np,H}^j}$, compute $G(x; x_k^s)$ and $\nabla_{x^s} G(x; x_k^s)$ by Step 6 of Algorithm 2, and evaluate $u^{\text{tot}}(x)$ by using the trapezoidal rule, with the set of nodes $\tilde{\Gamma}_{\text{num}}$, to discretize

$$u^{\text{tot}}(x) = \int_{\tilde{\Gamma}} [\partial_{\nu(y)} G(x; y) u^{\text{tot}}(y) - G(x; y) \partial_\nu u^{\text{tot}}(y)] ds(y).$$

Throughout Algorithms 3 and 4, we observe that the background Green's function $G(x; y)$ is evaluated for $x \in \tilde{\Gamma} \cup (\cup_{j \in \mathbb{Z}} \partial\Omega_{p,H}^j)$ and $y \in \tilde{\Gamma}$. Owing to the IFB transform (9) and the quasi-periodicity of G_α^{qp} , it is enough to evaluate $G_\alpha^{qp}(x; y)$ for $x \in \tilde{\Gamma} \cup \partial\Omega_{p,H}^0$, $y \in \tilde{\Gamma}$, and $\alpha \in \{\alpha_j\}_{j=1}^n$ only. This is the fundamental feature that accounts for the efficiency of the proposed solver!

We make two remarks to conclude this section.

Remark 4.1. We have assumed so far that only one cell is perturbed. In fact, the current approach can handle more general situations. For example, when there are two perturbed cells that are far apart, the scattering problem becomes numerically challenging to solve if we use a single large curve $\tilde{\Gamma}$ to enclose both perturbed regions. Instead, we can use two separate smaller curves, each enclosing the perturbed region within its respective cell, as illustrated in Figure 7. By

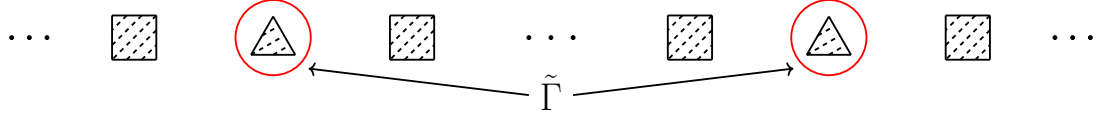


Figure 7: Two far apart, perturbed unit cells.

setting $\tilde{\Gamma}$ as the union of the two separate curves, we can follow exactly the same procedures to compute the wavefield in all cells. This should be compared with [25, 16]. The numerical solvers therein are based on two marching operators to truncate the periodic direction, and have to discretize all cells between the two perturbed cells before computing the wavefield everywhere.

Remark 4.2. If $x^* \notin \Omega_b$, certainly, we can follow the same approach as in Remark 4.1, using an extra closed curve to enclose the source point x^* . However, discretizing this extra curve increases the computational burden. To resolve this issue, we redefine $u^{\text{og}}(x; x^*) = u^{\text{tot}}(x; x^*) - G(x; x^*)$ for $x \notin \Omega_b$, where $G(x; x^*)$ is evaluated by Algorithms 1 and 2, and the current approach can be easily adapted to compute u^{tot} .

5. Numerical examples

In this section, we carry out several numerical experiments to validate the proposed numerical solver. To illustrate the accuracy of the method, we first compute the wavefield u^{tot} on the artificial curve $\tilde{\Gamma}$ for some sufficiently large n , M and N , where we recall that n is the number of nodes in the discretized IFB transform (13), M is the total number of grid points on the obstacle boundary Γ_{np}^j in the j -th unit cell, and N is the total number of grid points on the rectangular boundary $\partial[(2\pi j - \pi, 2\pi j + \pi) \times (-H, H)]$. Then, we compare it with the less accurate numerical solutions for some smaller values of n , M or N , at a common set of grid points on $\tilde{\Gamma}$ by checking the relative error

$$E_{\text{rel}} = \frac{\|u_{\text{num}}^{\text{tot}} - u_{\text{ref}}^{\text{tot}}\|_{\infty}}{\|u_{\text{ref}}^{\text{tot}}\|_{\infty}},$$

where $u_{\text{ref}}^{\text{tot}}$ denotes the vector of the reference solution on $\tilde{\Gamma}$ and $u_{\text{num}}^{\text{tot}}$ denotes the vector of a numerical solution to be compared.

We shall demonstrate the performance of the current solver for two different wavenumbers $k = 1.25$ and $k = 1.5$, and compare it with our recently proposed PML-BIE solver [25], as [31] hints a poorer performance of the PML truncation for half-integers. In all examples, we assume the period is 2π , take $p = 6$ in (32), and use $\tilde{N}_p = 300$ points to discretize the artificial curve $\tilde{\Gamma}$, which ensures that the discretization error for the TBC is sufficiently small.

Example 1. In this example, the obstacles are disks of radius 2 and one of them is replaced by a drop-shaped obstacle, with the boundary $\{x = (1.8 \sin(t), 3.6 \sin(\frac{1}{2}t) + 1.8), 0 \leq t \leq 2\pi\}$. The boundaries of these obstacles are illustrated by the solid lines in Figure 8. We compute the total wavefield u^{tot} excited by a source at $x^* = (2.2, 0)$.

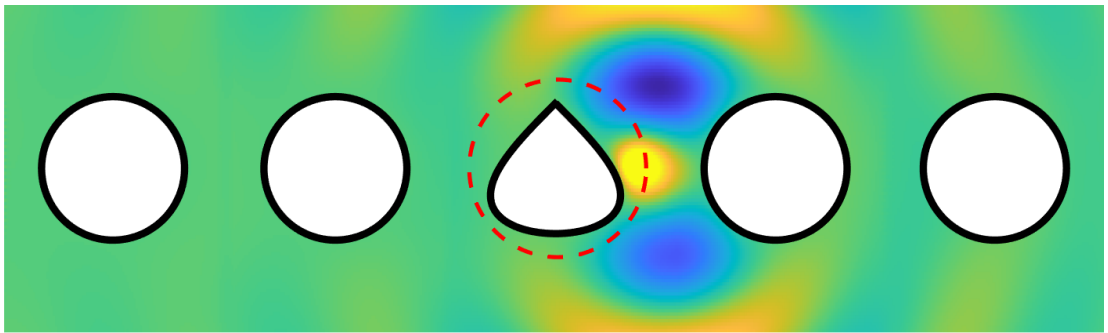


Figure 8: Example 1: Real part of u^{tot} for $k = 1.25$.

As illustrated by the dashed lines in Figure 8, the artificial curve $\tilde{\Gamma}$ is chosen as a circle of radius 2.5 centered at $(0, 0)$ that encloses the drop-shaped obstacle. By choosing $H = \pi$, $M = 150$, $N = 600$, we compute the total wavefield u^{tot} for the wavenumber $k = 1.25$ with $n = 32$ in (13) and for the wavenumber $k = 1.5$ with $n = 18$, and obtain two reference solutions; note that for the half-integer wavenumber, the IFB transform involves a single integral so that a fewer number of discretization points are needed. The field pattern of the reference solution for $k = 1.25$ in five consecutive cells is shown in Figure 8. We evaluate E_{rel} by comparing the numerical solutions with the reference solutions at 300 uniformly spaced grid points on $\tilde{\Gamma}$ for different values of n . The convergence curves for the two different wavenumbers are shown in Figure 9(a).

To apply the PML-BIE solver [25], we place two PMLs above $x_2 = H$ and below $x_2 = -H$, and evaluate the total wavefield u^{tot} on $\tilde{\Gamma}$ using exactly the same number of points on the boundary of each unit cell in the physical domain. Based on the computed two reference solutions, we evaluate E_{rel} for the PML solutions for different values of PML thickness. The corresponding convergence curves for the two different wavenumbers are shown in Figure 9(b).

Compare Figures 9 (a) and (b). When k is not a half-integer, both methods can provide roughly 12 accurate digits. However, we find that the current method takes only 40 seconds, while the PML-BIE method takes more than 4 minutes. When k is a half-integer, the PML-BIE method provides only 7 accurate digits for the same thickness and its convergence rate downgrades significantly. Nevertheless, the current method can still provide 12 accurate digits. In Figure 10(a), we also show the running times T_{na} for solving the non-quasi-periodic problem with $n = 32$ and

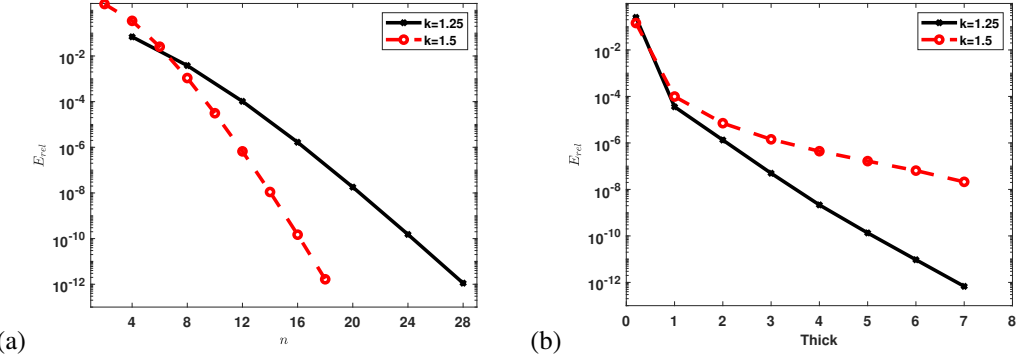


Figure 9: Example 1: (a) E_{rel} against n for $k = 1.25, 1.5$ based on the current method; (b) E_{rel} against n for $k = 1.25, 1.5$ based on the PML-BIE method [25].

$N_p = 300$ and T_q for solving one single quasi-periodic problem, for different values of $M + N$. It can be seen that the running time of the non-quasi periodic problem is only about twice that of one quasi periodic problem for sufficiently large $M + N$, demonstrating the efficiency of the current solver. Figure 10(b) shows the variation of T_{nq} for different values of n with $N + M = 1500$ and $N_p = 300$. It can be seen that T_{nq} does not increase in direct proportion to n . Instead, an eightfold increase in n results in a less than twofold increase in T_{nq} only.

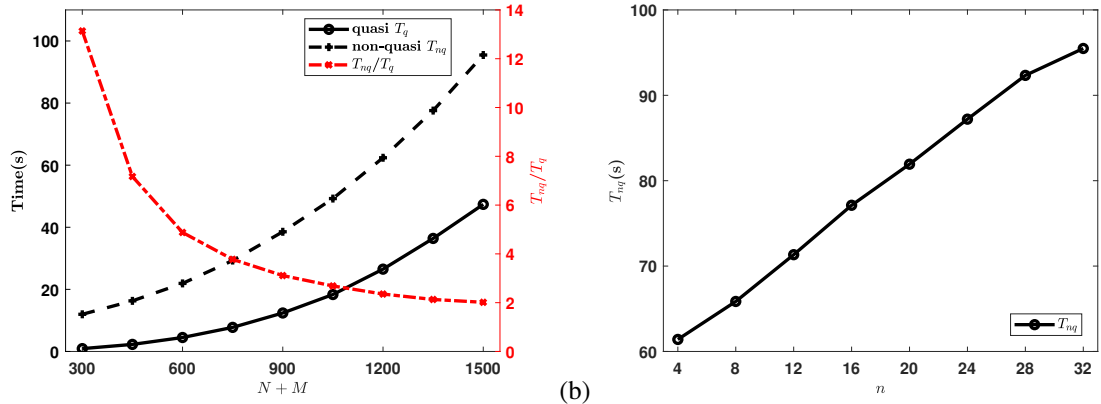
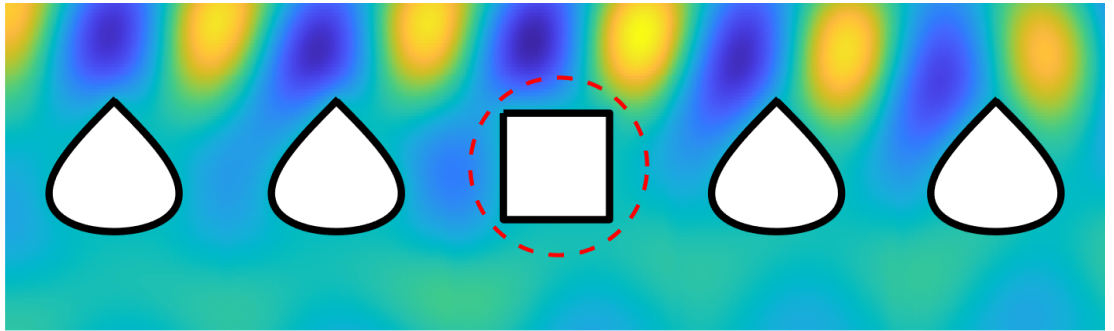
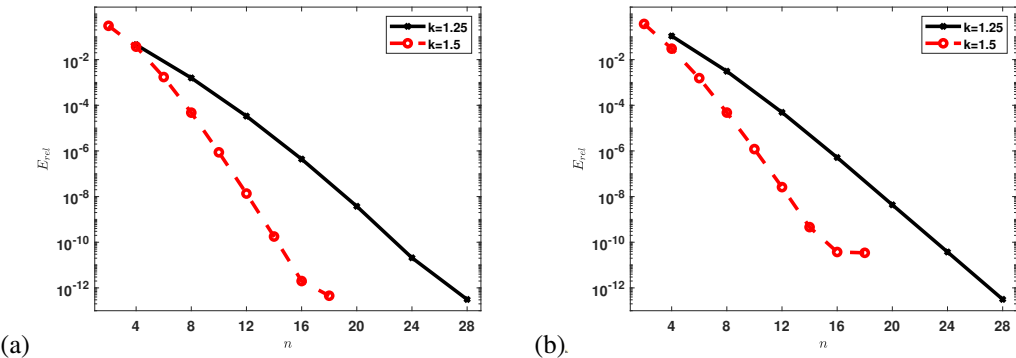
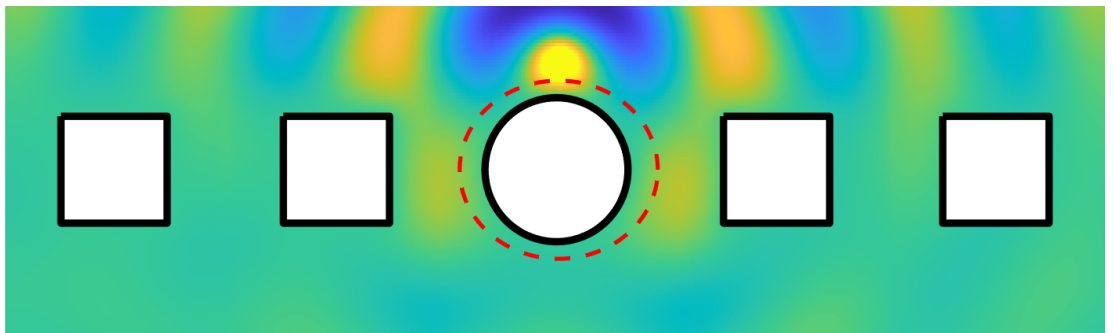


Figure 10: Example 1: (a) Running times T_{nq} and T_q for the non-quasi-periodic problem and a quasi periodic problem against $N + M$; (b) T_{nq} against n .

Example 2. In this example, we use the drop-shaped obstacle in Example 1 to construct a 2π -periodic structure and replace one of them by a square obstacle with a side length of 3, as illustrated by the solid lines in Figure 11. We compute the total wavefield u^{tot} excited by a plane wave $e^{ik(\cos \theta x_1 - \sin \theta x_2)}$ with the incident angle $\theta = \frac{\pi}{6}$. As illustrated by the dashed lines in Figure 11, the artificial curve $\tilde{\Gamma}$ is also chosen as a circle of radius 2.5 that encloses the square obstacle. By choosing the same parameters H , M , N and n as example 1, we compute reference solutions of the total wavefield u^{tot} for two different wavenumbers $k = 1.25$ and $k = 1.5$. The field pattern of $\Re(u^{\text{tot}})$ for $k = 1.25$ in five consecutive cells is shown in Figure 11.

We evaluate E_{rel} by comparing the numerical solutions with the reference solutions at 300 grid points on $\tilde{\Gamma}$ for different values of n . The convergence curves for the two different wavenumbers are shown in Figure 12(a).

Example 3. In this example, we use the square obstacle in Example 2 to produce a 2π -periodic structure and replace one of them by a disk of radius 2, as illustrated by the solid lines in Figure 13. We compute the total wavefield u^{tot} excited by a source $x^* = (0, 3)$. As illustrated by the dashed lines in Figure 13, the artificial curve $\tilde{\Gamma}$ is chosen as an ellipse with a major axis of 5.6 in x_1 -direction and a minor axis of 5 in x_2 -direction that encloses the disk obstacle. By

Figure 11: Example 2: Real part of u^{tot} for $k = 1.25$.Figure 12: (a) E_{rel} against n for $k = 1.25, 1.5$ for Example 2; (b) E_{rel} against n for $k = 1.25, 1.5$ for Example 3.Figure 13: Example 3: Real part of u^{tot} for $k = 1.25$.

choosing $H = \pi$, $M = 600$ and $N = 600$, and $n = 32$ for $k = 1.25$ and $n = 18$ for $k = 1.5$, we obtain two reference solutions. The field pattern of $\Re(u^{\text{tot}})$ for $k = 1.25$ in five consecutive cells is shown in Figure 13. We evaluate E_{rel} by comparing numerical solutions with the reference solution at 300 grid points on $\tilde{\Gamma}$ for different values of n . The convergence curves for the two different wavenumbers are shown in Figure 12(b).

6. Conclusion

In this paper, we have developed a new BIE method based on the FB transform for solving an acoustic wave scattering problem in a locally perturbed periodic structure in two dimensional spaces. Adopting the FB and IFB transforms, we developed efficient algorithms for computing the Green's functions and its derivatives for the

background periodic structure. These Green's functions helped to construct a BIE on an artificial curve enclosing the perturbation, serving as a TBC to truncate the unbounded domain. The BIE was discretized by a spectral accuracy quadrature rule. Effective algorithms based on leap and pullback procedures were further developed to compute the total wavefield everywhere in the structure. Numerical experiments have demonstrated the efficiency and accuracy of this new method.

The method can be extended towards a number of directions. For periodic obstacles that are sound-hard or penetrable, and for periodic surfaces used in diffraction gratings, as long as there are no guided modes, this approach can be extended to construct the TBC. In particular, when the periodic structure contains unbounded periodic interfaces, the TBC will be defined across different homogeneous media, making the background Green's function more difficult to evaluate in the vicinity of the interfaces. On the other hand, if guided modes indeed exist, the contour deformation approach for the IFB transform in [29], constructing a new path to detour the guided modes, can be used to construct the TBC. Nevertheless, we are more interested in dealing with the real-path integrals with integrands of poles directly [17], as such poles cannot be detoured for locally perturbed bi-periodic structures in three dimensions [2]. We wish to tackle these issues in the future.

Acknowledgment

This work was done when the second author K. Shen was visiting the third author R. Zhang at TU Berlin. Shen is grateful to Prof. Zhang for her kind help and insightful supervision during the visit. W. Lu is partially supported by the National Key Research and Development Program of China (2024YFA1012600, 2023YFA1009100), China NSF grant 12174310, and a Key Project of Joint Funds for Regional Innovation and Development (U21A20425), Zhejiang Provincial NSF Distinguished Youth Program (Extended Program LRG25A010001).

References

- [1] Alpert, B.K., 1999. Hybrid Gauss-trapezoidal quadrature rules. *SIAM Journal on Scientific Computing* 20, 1551–1584.
- [2] Arens, T., Shafeeabeyaneh, N., Zhang, R., 2024. A high-order numerical method for solving non-periodic scattering problems in three-dimensional bi-periodic structures. *ZAMM-Journal of Applied Mathematics and Mechanics/Zeitschrift für Angewandte Mathematik und Mechanik* 104, e202300650.
- [3] Bao, G., Dobson, D., Cox, J., 1995. Mathematical studies in rigorous grating theory. *Journal of the Optical Society of America A* 12, 1029–1042.
- [4] Bao, G., Li, P., 2022. *Maxwell's Equations in Periodic Structures*. Springer.
- [5] Barnett, A., Greengard, L., 2011. A new integral representation for quasi-periodic scattering problems in two dimensions. *BIT Numerical mathematics* 51, 67–90.
- [6] Berenger, J.P., 1994. A perfectly matched layer for the absorption of electromagnetic waves. *J. Comput. Phys.* 114, 185 – 200.
- [7] Bonnet-Bendhia, A., Starling, F., 1994. Guided waves by electromagnetic gratings and non-uniqueness examples for the diffraction problem. *Mathematical Methods in the Applied Sciences* 17, 305–338.
- [8] Bruno, O., Fernandez-Lado, A., 2020. On the evaluation of quasi-periodic Green functions and wave-scattering at and around Rayleigh-Wood anomalies. *J. Comput. Phys.* 410, 109352, 24.
- [9] Chandler-Wilde, S.N., Monk, P., 2009. The PML for rough surface scattering. *Applied Numerical Mathematics* 59, 2131–2154.
- [10] Colton, D., Kress, R., 2013. *Inverse Acoustic and Electromagnetic Scattering Theory* (3rd Edition). Springer.
- [11] Ehrhardt, M., Han, H., Zheng, C., 2008. Numerical simulation of waves in periodic structures. WIAS.
- [12] Helfert, S., Pregla, R., 1998. Efficient analysis of periodic structures. *Journal of Lightwave Technology* 16, 1694.
- [13] Hsu, C., Zhen, B., Stone, A., Joannopoulos, J., Soljačić, M., 2016. Bound states in the continuum. *Nature Reviews Materials* 1, 1–13.
- [14] Hu, G., Kirsch, A., 2024. Time-harmonic scattering by locally perturbed periodic structures with Dirichlet and Neumann boundary conditions. arXiv preprint arXiv:2402.11230 .
- [15] Hu, Z., Lu, Y.Y., 2009. Efficient numerical method for analyzing coupling structures of photonic crystal waveguides. *IEEE Photonics Technology Letters* 21, 1737–1739.
- [16] Joly, P., Li, J.R., Fliss, S., 2006. Exact boundary conditions for periodic waveguides containing a local perturbation. *Commun. Comput. Phys* 1, 945–973.
- [17] Kirsch, A., Lechleiter, A., 2018. The limiting absorption principle and a radiation condition for the scattering by a periodic layer. *SIAM Journal on Mathematical Analysis* 50, 2536–2565.
- [18] Lechleiter, A., 2017. The Floquet–Bloch transform and scattering from locally perturbed periodic surfaces. *Journal of Mathematical Analysis and Applications* 446, 605–627.
- [19] Lechleiter, A., Zhang, R., 2017. A Floquet–Bloch transform based numerical method for scattering from locally perturbed periodic surfaces. *SIAM Journal on Scientific Computing* 39, B819–B839.
- [20] Lu, W., Lu, Y.Y., 2012a. Efficient boundary integral equation method for photonic crystal fibers. *J. Lightwave Technol.* 30, 1610–1616.
- [21] Lu, W., Lu, Y.Y., 2012b. High order integral equation method for diffraction gratings. *JOSA A* 29, 734–740.
- [22] Lu, W., Lu, Y.Y., 2014. Efficient high order waveguide mode solvers based on boundary integral equations. *J. Comput. Phys.* 272, 507 – 525.

- [23] Sun, J., Zheng, C., 2008. Numerical scattering analysis of te plane waves by a metallic diffraction grating with local defects. *Journal of the Optical Society of America A* 26, 156–162.
- [24] Wu, Y., Lu, Y.Y., 2011. Boundary integral equation Neumann-to-Dirichlet map method for gratings in conical diffraction. *Journal of the Optical Society of America A* 28, 1191–1196.
- [25] Yu, X., Hu, G., Lu, W., Rathsfeld, A., 2022. PML and high-accuracy boundary integral equation solver for wave scattering by a locally defected periodic surface. *SIAM Journal on Numerical Analysis* 60, 2592–2625.
- [26] Yuan, L., Lu, Y.Y., 2007. A recursive-doubling Dirichlet-to-Neumann-map method for periodic waveguides. *Journal of Lightwave Technology* 25, 3649–3656.
- [27] Zhang, B., Zhang, R., 2018. An FFT-based algorithm for efficient computation of green's functions for the helmholtz and maxwell's equations in periodic domains. *SIAM Journal on Scientific Computing* 40, B915–B941.
- [28] Zhang, R., 2018. A high order numerical method for scattering from locally perturbed periodic surfaces. *SIAM Journal on Scientific Computing* 40, A2286–A2314.
- [29] Zhang, R., 2021. Numerical methods for scattering problems in periodic waveguides. *Numerische Mathematik* 148, 959–996.
- [30] Zhang, R., 2022a. Exponential convergence of perfectly matched layers for scattering problems with periodic surfaces. *SIAM Journal on Numerical Analysis* 60, 804–823.
- [31] Zhang, R., 2022b. Fast convergence for of perfectly matched layers for scattering with periodic surfaces: the exceptional case. *arXiv preprint arXiv:2211.01229* .